Time-Domain Wideband Adaptive Beamforming for Radar Breast Imaging

Dallan Byrne and Ian J. Craddock

***Abstract*—A novel wideband microwave radar imaging method is presented to detect regions of significant dielectric contrast within the breast. Clutter reduction is paramount to any radar imaging algorithm, especially with clinical patient data where the tissue composition of the breast is inhomogeneous. Time-domain data-adaptive imaging methods have been previously applied in a narrowband manner for microwave radar breast imaging when the received signal spectral content was wideband. In this study, a wideband time-domain adaptive imaging approach is presented to perform data-adaptive focusing across the spectrum to reduce clutter. An equalization filter is adapted to compensate for the propagation distortion through tissue using a calculated estimate of the average dielectric properties of the breast. The effectiveness of the proposed wideband adaptive imaging approach is evaluated in conjunction with the delay-and-sum (DAS) method using numerical, experimental, and clinical data. Target scatterers are clearly detected while clutter levels are reduced significantly, between 4 and 6 dB, when compared to the DAS technique.**

***Index Terms*—Beamforming, biomedical radar imaging, microwave imaging, ultra-wideband.**

I. Introduction

In recent years, there have been several applications of microwave imaging toward the breast screening problem. An informative overview can be found in [1] and [2]. A microwave imaging system illuminates the breast with a wideband pulse. Scatterings occur within the breast due to the electromagnetic reflections generated at tissue boundaries where there is a significant contrast in permittivity and conductivity. Spatial information that details internal tissue structure is retrieved through recorded scatterings via an array of receivers. Within the microwave imaging domain, there are two main techniques that exploit this scattering effect; tomographic and radar imaging. While tomography attempts to quantitatively reconstruct the dielectric profile of the breast via the inverse solution [3], [4], radar imaging offers a qualitative representation of the electromagnetic scatterings which occur between dielectrically varying tissues [5]–[7].

In a typical radar application, an antenna array collects spatial samples of propagating wave fields which are processed by a receive beamformer, which spatially filters the data to identify the signal from a desired direction and mitigate unwanted noise and interference [8]. In the context of radar breast imaging, the desired signal is the constituent of the scattered field originating from the point in space represented by a particular focal point. Documented receive beamforming methods, in a breast imaging context, involve time-shifting, weighting, and summing the backscattered signals from the breast to determine the spatial location of any dielectric scatterer present. These methods produce an output radar energy profile of the breast, aiming to maximize the ratio between scatterings from suspicious regions and clutter. Clutter in this sense may represent reflections from low-contrast tissue boundaries and multipath propagation through the breast.

Within the literature, radar image formation techniques can be decomposed into two beamforming categories based on the mode of weight calculation; data-independent (DI) and data-adaptive (DA) algorithms. The weights of a DI beamformer are designed to approximate a desired response irrespective of the received signal properties. An example is the popular delay-and-sum (DAS) algorithm where backscattered signals are time-shifted and summed to create a synthetic focus [9]–[11] based on an assumed propagation path. To counter the dispersive effects of breast tissue, Bond *et al.* [12] developed a wideband channel equalization filter with a monostatic array configuration, labeled the microwave-imaging space–time (MIST) beamformer. The propagation channel was approximated using the attenuation and phase constant associated with the assumed average dielectric properties of the breast. More recently, the MIST beamformer has been modified toward frequency-domain processing of measurement data [13] and using a multistatic array configuration [14].

In contrast to DI algorithms, the weights of a DA beamformer are calculated from the second-order statistics, e.g., variance, of the received signal data to mitigate the influence of noise and clutter [8]. The Capon beamformer, also termed the minimum variance distortionless response (MVDR) method, calculates beamformer weights to minimize the output power across the array while limiting the beamformer response to allow signals from the desired direction to pass with specified phase and gain [8], [15]. The first application of a DA method for breast imaging was outlined and evaluated using numerical simulation data by Xie *et al.* [16] and, subsequently, validated with measurement data by Klemm *et al.* [17]. However, in both studies, the time-domain signal data were processed using a narrowband beamforming architecture, despite the dispersive nature of the breast tissues which present [18]. To the best of the author's knowledge, there has been no documented application of a wideband adaptive imaging algorithm with simulated or measured data.

Manuscript received May 28, 2014; revised December 15, 2014; accepted January 26, 2015. Date of publication January 29, 2015; date of current version April 03, 2015.

The authors are with the Department of Electrical and Electronic Engineering, University of Bristol, Bristol, U.K. (e-mail: Dallan.Byrne@bristol.ac.uk).

Color versions of one or more of the figures in this paper are available online at http://ieeexplore.ieee.org.

Digital Object Identifier 10.1109/TAP.2015.2398125

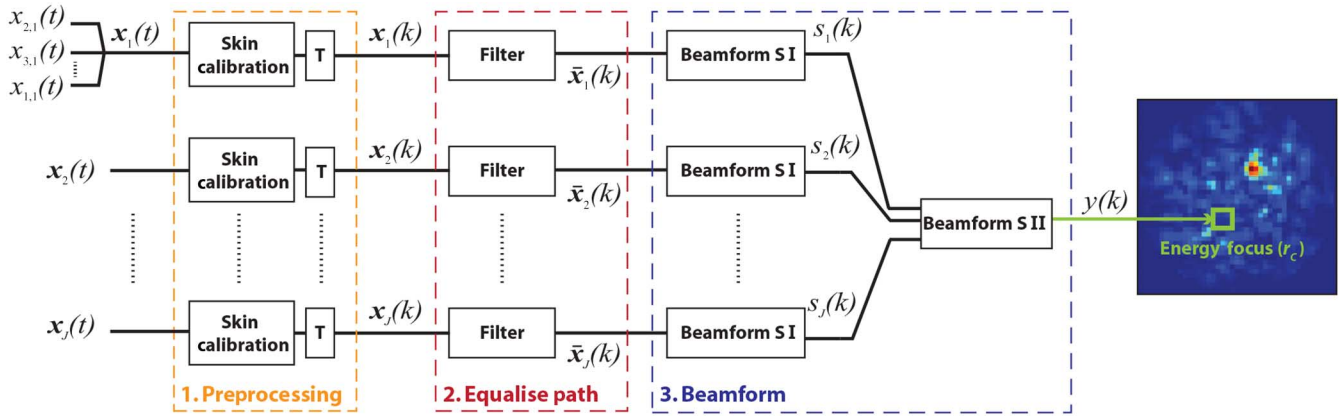

Fig. 1. Block diagram of the imaging algorithm.

In this paper, a wideband time-domain adaptive imaging method, outlined in Fig. 1, is proposed to improve the breast imaging capability of a microwave radar system. The proposed wideband imaging method consists of banks of equalization filters and a two-stage time-domain DA beamformer based on the MVDR architecture.

The key contributions of this study are as follows:

1) A DA method is proposed to apply weights across the full operational bandwidth of the system as opposed to the narrowband implementations documented in previous studies [16], [17].
2) Signal presteering and equalization compensation are based on a calculated estimate of the average permittivity of the breast, instead of an assumed *a priori* value.

Data preprocessing is outlined in Section II-A, and the wideband equalisation filters and DA beamformers are detailed in Sections II-B and II-C, respectively. A number of validation scenarios are detailed to highlight the versatility of the method with differing operating bandwidths, array geometries, imaging scenarios, and noise levels. Numerical MRI-derived phantom results are outlined in Section III. Section IV describes a number of experimental phantoms and the results generated using a physical array. Patient data, taken from a clinical study, are evaluated and presented in Section V. Concluding remarks are given in Section VI.

II. Imaging Methods

A synthetic postscan wideband focusing algorithm is described within this section and illustrated in Fig. 1, beginning with data preprocessing, then providing an overview of the equalization filter and finally describing the time-domain DA beamformer. In a multistatic radar acquisition system with I transmitters and J receivers, the recorded data are denoted by $x_{ij}(t)$ at the tth sample for the ith transmitter and jth receiving element.

With regards to notation, $\boldsymbol{x}$ represents a column vector while $\mathbf{X}$ denotes a matrix. $\mathbf{1}_N$ is a column vector of length N and populated with ones, $\odot$ is the elementwise product and $\otimes$ is the Kronecker product operator.

A. Preprocessing

In Fig. 1, $\mathbf{x}_j(t)$ denotes signal data pertaining to all transmitted signals received at antenna element j. Scattering from the skin-breast boundary and coupling between antenna elements inhibits the detection of internal breast scatterers. While any number of documented skin and coupling calibration algorithms can be used in conjunction with the proposed imaging method [2], [12], the authors implement a mechanical differential scanning skin calibration technique to remove the influence of the skin; a second scan is performed with a 10° rotation of the antenna array and residual data are obtained via subtraction. Undesirable skin and coupling artefacts will be suppressed if the skin contour remains relatively consistent throughout the specified rotation. The choice of rotation angle was detailed in a previous study [17] and found, in practice, to work well for ellipsoid targets placed in homogeneous phantoms. In reality, there is no optimal choice for the skin calibration rotation angle as an exact parameter would require unavailable *a priori* knowledge of the breast tissue density, target size, and location. However, the skin contour will rarely be perfectly hemispherical and experience has shown that larger rotation angles can result in inadequate skin reflection suppression. The authors acknowledge that the method is far from ideal as the internal breast scattering can become distorted during the process but have found the differential rotation calibration method to be more effective than other methods in the literature when mitigating skin reflections with multistatic measurement data.

Antennas with broadside illumination relative to a particular focal points are given a higher priority in the reconstruction while elements which do not adequately illuminate the focus influence less. Signals originating or received at a particular antenna are weighted according to the angular distance between each focal point and antenna broadside. This is achieved using an apodization weighting function. For a bistatic signal, the relative angle between the focal point and the transmitter and the angle between focal point and receiving a will dictate a weight to determine the signal's contribution at this focus in the energy profile. The shape of the tapered window in Fig. 2, consistent for all antenna elements and breast sizes, has been

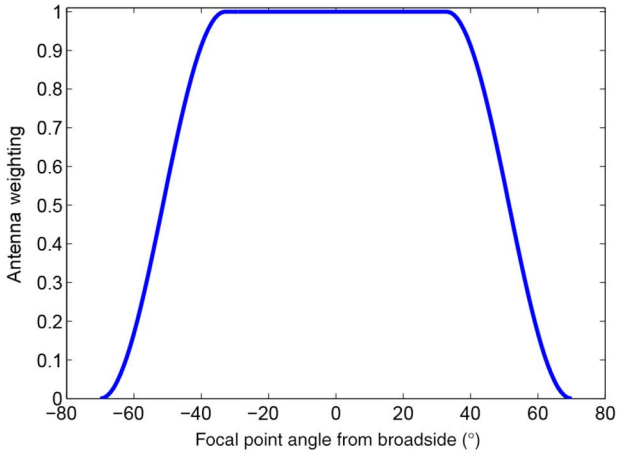

Fig. 2. Apodization weighting for any antenna with 0° indicating broadside.

approximated to reflect the simulated beampattern and fidelity measurements of the measurement antenna [19].

All signals are presteered based on the estimated time delay T_{ij} from the transmitter location $\mathbf{r}_i$ to the synthetic focal point $\mathbf{r}_C$ and on to the receiver position $\mathbf{r}_j$. This delay requires an *a priori* estimate of the speed of propagation through breast tissue, a quantity that was previously assumed to represent fatty tissue [10]–[12], [16]. However, the breast is a dielectrically heterogeneous entity and within this study the authors instead employ a time-of-flight (ToF) method developed by Sarafianou *et al.* [20] to calculate an estimate of the relative permittivity ϵ_{est} and hence, the average speed of the propagation channel within the breast. Permittivity values are calculated at three distinct frequencies, where the input data are band limited around each frequency of interest. A polynomial fitting method is used to interpolate between each permittivity value and provide an estimate of ϵ_{est} across the system bandwidth. Conductivity values are matched empirically to each permittivity estimate from the dielectric recordings in [18] and [21]. Each delayed signal is denoted as $x_{ij}(k)$, where $k = t + T_{ij}$ and the delayed group is denoted by $\mathbf{x}_j(k)$.

B. Equalization

The preprocessed signal data, $\mathbf{x}_j(k)$ in Fig. 1, are now equalized by compensating for both attenuation and phase errors. An L-tap FIR equalization filter is adapted from the data-independent MIST beamformer [12], [22] and reproduced here for completeness. $\mathbf{x}_j$ are converted to stacked-tap form in order to apply the equalized inputs to a tapped-delay line architecture

$$\dot{\mathbf{x}}_j(k) = \left[\mathbf{x}_{j1}^T(k), \mathbf{x}_{j2}^T(k), \ldots, \mathbf{x}_{jL}^T(k)\right]^T \tag{1}$$

where $\mathbf{x}_{jl}$ denotes the $I \times 1$ array signal data after the $(l-1)$ tap.

The frequency response of the FIR filter [22] for the channel ij can be defined as

$$h_{ij}(\mathbf{r}_C, f) = \mathbf{w}_{ij}^H a_{ij}(\mathbf{r}_C, f) = \sum_{l=0}^{L-1} w_{ij}^H(l) e^{-j\omega\Delta T l} \tag{2}$$

where H depicts the Hermitian transpose, ΔT is the time resolution, f is the frequency, and $\boldsymbol{a}_{ij}$ represents the array response vector. We attempt to calculate $\dot{\boldsymbol{w}}_E$, the $IL \times 1$ tapped stacked vector denoted by

$$\dot{\boldsymbol{w}}_E = \left[\mathbf{w}_{j1}^T, \mathbf{w}_{j2}^T, \ldots, \mathbf{w}_{jL}^T\right]^T. \tag{3}$$

$\dot{\boldsymbol{a}}_E = [\mathbf{a}_{j1}^T, \mathbf{a}_{j2}^T, \ldots, \mathbf{a}_{jL}^T]^T$ is the stacked tapped array response vector for all channels and can be denoted as

$$\dot{\boldsymbol{a}}_E(\mathbf{r}_C, f) = \begin{bmatrix} P_{2j}(\mathbf{r}_C, f)\mathbf{d}(f) \\ P_{3j}(\mathbf{r}_C, f)\mathbf{d}(f) \\ \vdots \\ P_{Ij}(\mathbf{r}_C, f)\mathbf{d}(f) \end{bmatrix} \tag{4}$$

$$\mathbf{d}(f) = [1, e^{-j\omega\Delta T}, \ldots, e^{-j\omega(L-1)\Delta T}]^T. \tag{5}$$

$\dot{\boldsymbol{a}}_E$ is modified to incorporate the propagation of an electromagnetic wave through biological tissue. The propagation model is defined as

$$P_{ij}(\mathbf{r}_C, f) = e^{-\alpha(f)\mathbf{d}_{ij}} e^{-j\beta(f)\mathbf{d}_{ij}} \tag{6}$$

where the Euclidean distance of propagation to $\mathbf{r}_C$ is denoted as $\mathbf{d}_{ij}$. $\alpha(f)$ and $\beta(f)$ are the frequency-specific attenuation and phase constants, respectively. In previous studies, these values were based on an assumed estimate of the dielectric properties of breast tissue across a specified frequency band [12]–[14]. In this study, we derive $\alpha(f)$ and $\beta(f)$ across the operational bandwidth using ϵ_{est} (Section II-A).

Filter coefficients $\dot{\mathbf{w}}_E$ are designed to minimize the sum of the squared differences (L_2 norm) between the desired (h_{des}) and actual filter response. The overdetermined linear least squares problem can be written as

$$\min_{\dot{\mathbf{w}}_E} \left|\dot{\mathbf{w}}_E^H \mathbf{A} - \mathbf{h}_{\text{des}}\right|^2 \tag{7}$$

where

$$\mathbf{A} = [\dot{\boldsymbol{a}}_E(\mathbf{r}_C, f_1), \dot{\mathbf{a}}_E(\mathbf{r}_C, f_2), \ldots, \dot{\boldsymbol{a}}_E(\mathbf{r}_C, f_{N_f})] \tag{8}$$

$$\mathbf{h}_{\text{des}} = [e^{-j\omega_1\Delta T(L-1)/2}, \ldots, e^{-j\omega_{N_f}\Delta T(L-1)/2}] \tag{9}$$

where $\omega = 2\pi f$ and N_f is the number of frequency samples. $\dot{\mathbf{w}}_E$ can be obtained from a linear solution to (7) which is clearly outlined in [12], [15], and [22] and described as

$$\dot{\mathbf{w}}_E = (\mathbf{A}\mathbf{A}^H)^{-1}\mathbf{A}\mathbf{h}_{\text{des}}^H. \tag{10}$$

The output of the tap-stacked equalization filter can be described as

$$\bar{\mathbf{x}}_j(k) = \dot{\mathbf{w}}_E \odot \dot{\mathbf{x}}_j(k). \tag{11}$$

C. Data-Adaptive Beamforming

Finally, $\bar{\mathbf{x}}_j(k)$ is processed using a wideband DA algorithm. MVDR methods are known to outperform DI methods providing that self-nulling does not occur, i.e., the desired signal component is absent from the snapshots used to construct the

sample covariance matrix [23]. To overcome the self-nulling of the desired signal component, robustness can be achieved through diagonal loading techniques which modify the eigen-decomposition of the output variance [24]. In this paper, we apply a wideband time-domain DA beamformer based on the MVDR method. Robustness against self-nulling is achieved using a worst-case performance optimization-based method [23], [25], which has been shown to equate to the algorithm in [16] with optimum diagonal loading levels [26].

As illustrated in Fig. 1, there is a two-stage beamforming process to obtain a waveform $y(k)$ corresponding to the desired component at a synthetic focus.

1) In stage I, a desired wave component $s_j(k)$ is obtained for all transmitters contributing to a particular receiving antenna.
2) All desired wave components are processed in stage II to produce $y(k)$.

Although wideband processing can be achieved within the frequency domain, the number of time samples required to obtain sufficient resolution in the DFT representation reduces the number of snapshots available to construct the sample covariance matrix [15]. The following algorithm is reproduced from [25], [27], and [28] and included for completeness.

The stage I wideband adaptive beamforming filter will estimate the desired wave component $s_j(k)$ for all transmitted signals recorded at receiver j. The output of the beamformer is denoted as

$$s_j(k) = \mathbf{w}_I^T \bar{\mathbf{x}}_j(k) \tag{12}$$

where $\mathbf{w}_I$ is the stacked-tap representation of $\mathbf{W}$, with W_{ml} denoting the specific filter weight for the mth signal after the $l-1$ tap.

The MVDR beamformer minimizes the output variance or noise of the system while maintaining a distortionless response towards the desired signal component and is formulated as

$$\min_{\mathbf{w}_I} \mathbf{w}_I^H \mathbf{R}_{\bar{\mathbf{x}}} \mathbf{w}_I \quad \text{subject to} \quad h_I(f) = 1 \tag{13}$$

where $h_I(f) = \mathbf{w}_I^H \mathbf{a}(\mathbf{r}_C, f)$ is the response of the beamformer to the desired signal component. The notation $\boldsymbol{a}(f)$ represents the array steering vector and will replace $\boldsymbol{a}(\mathbf{r}_C, f)$ from here on. MVDR-derived beamformers typically model statistical noise power using a covariance matrix containing only noise and interference. However, in many communications and radar imaging applications, such data are unavailable and the sample covariance matrix is constructed from received data snapshots in lieu of the noise covariance matrix [15]. $\mathbf{R}_{\bar{\mathbf{x}}}$ represents the covariance matrix, equated as $E\{\bar{\mathbf{x}}\bar{\mathbf{x}}^H\}$ and is calculated for this application as a sample covariance matrix across a number of predefined snapshots as

$$\mathbf{R}_{\bar{\mathbf{x}}} = \frac{1}{K} \sum_{n=k-K+1}^{k} \bar{\mathbf{x}}_j(n) \bar{\mathbf{x}}_j^H(n). \tag{14}$$

The worst-case performance optimization method outlined by Vorobyov *et al.* [23] add robustness to the MVDR by modeling the steering vector uncertainty as $\Delta(f) \triangleq \mathbf{a}(f) - \bar{\mathbf{a}}(f)$ where $\bar{\mathbf{a}}(f) = \mathbf{1}_I$ is the assumed steering vector, and placing an upper-bound of a known constant ρ on the $L2$ norm of $\Delta(f)$. In previous breast imaging applications of DA methods, $\Delta(f)$ was modeled as a constant and calculated at the center frequency of the system. In this paper, the steering vector uncertainty is assumed to vary across the operating bandwidth and is estimated for a number of discrete frequencies within the operating bandwidth. Now

$$\begin{aligned} &\min_{\mathbf{w}_I} \mathbf{w}_I^H \mathbf{R}_{\bar{\mathbf{x}}} \mathbf{w}_I \\ &\text{s.t.} \quad \left| \mathbf{w}_I^H \left(\bar{\mathbf{a}}(f) + \Delta(f) \right) \right| \geq 1 \quad \forall \, \|\Delta(f)\| \leq \rho. \end{aligned} \tag{15}$$

Distortionless response is maintained for the worst-case scenario or the value of $\Delta(f)$ which corresponds to the smallest value of $|\mathbf{w}_I^H(\bar{\mathbf{a}}(f) + \Delta(f))|$ while $\|\Delta(f)\| \leq \rho$.

The overall $IL \times 1$ array response vector within a wideband filter architecture can be formulated as

$$\hat{\mathbf{a}}(f) = \mathbf{d}(f) \otimes \left(\mathbf{T}(f) \mathbf{a}(f) \right). \tag{16}$$

The FIR beamformer response to the desired signal component can be written as

$$h_I(f) = \mathbf{w}_I^T \left[\mathbf{d}(f) \otimes \left(\mathbf{T}(f) \mathbf{a}(f) \right) \right] \tag{17}$$

with $\mathbf{T}(f) = \mathrm{diag}\{\mathrm{e}^{-\mathrm{j}\omega \mathrm{T}_{1\mathrm{j}}}, \ldots, \mathrm{e}^{-\mathrm{j}\omega \mathrm{T}_{\mathrm{I}\mathrm{j}}}\}$ representing the presteering delays $(T_{1j}, T_{2j}, \ldots, T_{Ij})$ and $\mathbf{d}(f)$ defined in (5). The array response or steering vector for the desired signal component is defined as

$$\mathbf{a}(f) = [e^{-j\omega\tau_{1j}}, \ldots, e^{-j\omega\tau_{Ij}}]^T \tag{18}$$

where τ_{ij} describes the actual delay from the desired signal source to $\mathbf{r}_i$. Presteering delays should be chosen to align the desired signal components at each sensor as $T_{ij} = T_0 - \tau_{ij}$ where T_0 ensures causality. Now the beamformer response in the case of perfect steering can be written as

$$h_I(f) = \mathbf{w}_I^T \left[(\mathbf{d}(f) \otimes \mathbf{1}_I) e^{-j\omega T_0} \right] \tag{19}$$

where $\mathbf{C}_0 = \mathbf{I}_L \otimes \mathbf{1}_I$.

In reality, the steering vector $\boldsymbol{a}(f)$ may contain errors due to presteering in accuracies and we can reformulate

$$\mathbf{T}(f) \boldsymbol{a}(f) = e^{-j\omega T_0} \mathbf{1}_I + \Delta(f) \tag{20}$$

where $\Delta(f)$ is the error vector pertaining to array response and delay quantisation inaccuracies. Now the beamformer response can be denoted as

$$\begin{aligned} h_I(f) = \\ e^{-j\omega T_0} \mathbf{w}_I^T (\mathbf{d}(f) \otimes \mathbf{1}_I) + \mathbf{w}_I^T (\mathbf{d}(f) \otimes \Delta(f)) \end{aligned} \tag{21}$$

Now (15) can be written as

$$\begin{aligned} &\min_{\mathbf{w}_I} \mathbf{w}_I^H \mathbf{R}_{\bar{\mathbf{x}}} \mathbf{w}_I \qquad \text{s.t.} \quad |h_I(f)| \geq 1 \\ &\forall \|\Delta(f)\| \leq \rho, \quad f \in [f_l, f_u]. \end{aligned} \tag{22}$$

In the absence of errors within the array manifold, distortionless response within the frequency range $[f_l, f_u]$ requires that

$$h_I(f) h_{\mathrm{Des}}^H(f) = 1 \tag{23}$$

where $h_{\rm des}(f)$ is the desired beamformer response for the signal of interest given by

$$h_{\rm des}(f) = e^{-j\omega\bar{T}} \tag{24}$$

where $\bar{T} = T_0 + (L-1)\Delta T/2$ is the time delay of $\bar{\mathbf{x}}_S$ at the output of the beamformer [25]. The resulting beamformer with combined magnitude and phase constraints can be written as

$$\begin{aligned} &\min_{\mathbf{w}_I} \mathbf{w}^H \mathbf{R}_{\bar{\mathbf{x}}} \mathbf{w} \\ &\text{s.t.} \quad \Re\left(h_I(f_k) e^{j\omega_k \bar{T}}\right) \geq 1 \\ &\forall \, \|\Delta(f_k)\| \leq \rho, \quad k = [1, \ldots, N_f]. \end{aligned} \tag{25}$$

The constraints in (25) limit both the magnitude and phase of the beamformer transfer function and the solution can be obtained using interior points methods [25]. Once the weights are obtained, they are applied to the input data via (12) to obtain $s_j(k)$, as shown in Fig. 1.

This process is repeated to obtain J waveform approximations $\mathbf{s}(k) = [s_1(k), s_2(k), \ldots, s_J(k)]^T$. The beamforming process is repeated to find weights $\mathbf{w}_S$ which satisfy (25) and result in the output waveform estimate for $\mathbf{r}_C$ is given as

$$y(k) = \mathbf{w}_{II}^T \mathbf{s}(k). \tag{26}$$

The energy is of $y(k)$ calculated across a window ($T_{\rm win}$) resulting in a qualitative energy value for $\mathbf{r}_C$, the voxel within the output three-dimensional (3-D) energy profile of the breast.

III. Numerical Validation

A. Data Acquisition

The proposed method is initially evaluated with simulated data, obtained with a finite-difference time-domain (FDTD) model based on an MRI-derived numerical breast phantom. A Class 2 (scattered fibroglandular) phantom [29] is mapped to a hemispherical profile, representing the model ground truth, and is illustrated in Fig. 3(c) and (d). A spherical malignant inclusion is inserted at $(x = 104\ \text{mm}, y = 58\ \text{mm}, z = 28\ \text{mm})$. All dielectric properties are based on studies by Lazebnik *et al.* [18], [21].

Thirty-one point sources are arranged in a conical array with three rings, as shown in Fig. 3(a) and (b). Each element is excited in turn with a single cycle sinusoid with a raised cosine envelope and center frequency of 3.2 GHz. The boundary of the FDTD domain is terminated using Mur absorbing boundary conditions. To obtain a differential image via array rotation, a second numerical dataset is obtained with the same phantom but with a rotational array offset of 10°. The rotated data are subtracted from the initial scan to provide differential signals which reduce the effects of coupling and skin reflections.

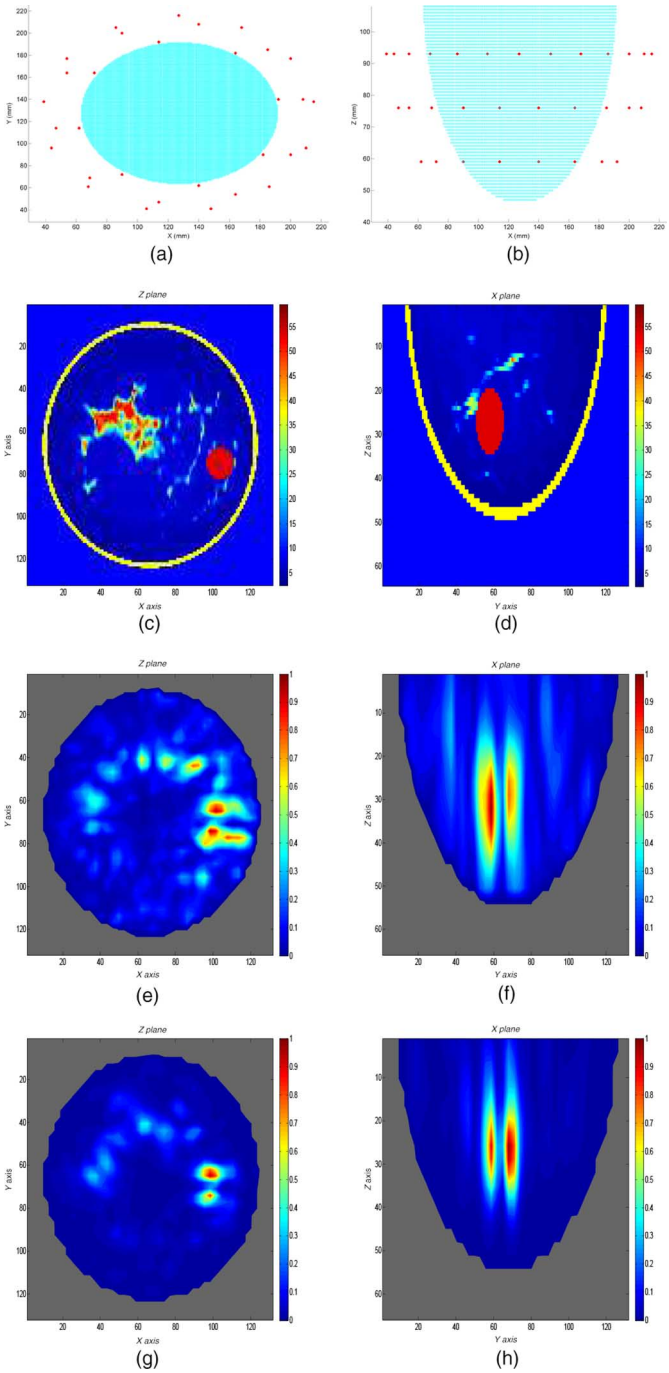

Fig. 3. Numerical imaging results. (a) 31 element conical array with the internal imaged breast coordinates: X–Z slice. (b) 31 element array and imaged breast coordinates: X–Y slice. (c) Ground truth: Z-slice. (d) Ground truth: X-slice. (e) DAS: Z-slice. (f) DAS: X-slice. (g) Proposed technique: Z-slice. (h) Proposed technique: X-slice.

B. Imaging Results

Images are created using the DAS algorithm to offer a benchmark to contrast with the wideband adaptive imaging method. For both algorithms a $T_{\rm win} = 0.9$ns window is used post delay calculation. In DAS, this window is used for summation and integration while in the wideband adaptive method, equalization filtering and DA beamforming are carried out across $T_{\rm win}$. For the proposed imaging method, ten samples were taken ($k = [0.2\,\text{ns}, 0.4\,\text{ns}, \ldots, 1\,\text{ns})$ with $K = 0.2\,\text{ns}$ snapshots, $T_0 = 0$ and $\rho = 0.9\|\mathbf{1}_I\|$. Filter lengths for the equalization filter and each beamforming filter are fixed at $L = 30$. These parameters

TABLE I
PEAK/MEAN METRIC RESULTS FOR THE SIMULATED DATA

Phantom	Peak/mean (dB)	
	Wideband adaptive	DAS
Class 3	14.81	9.69

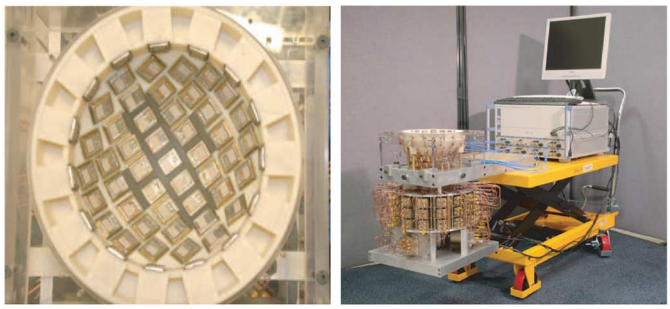

Fig. 4. Description of the experimental hardware: (a) illustrates the conformal array with antenna elements; while (b) shows the full Maria data acquisition system.

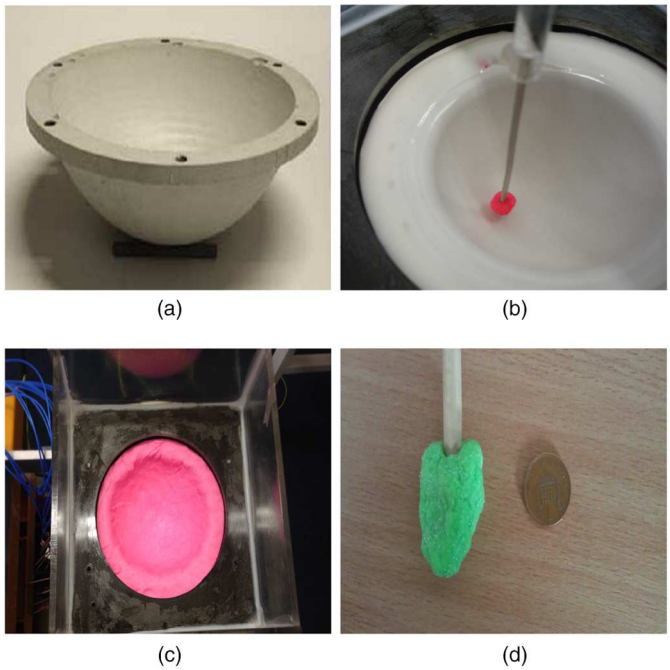

Fig. 5. Phantom illustrations. (a) Thin skin phantom. (b) Thin skin phantom with target placement. (c) Inhomogeneous skin phantom. (d) Tissue mimicking material which is placed adjacently to the target.

are maintained for measurement radar results, in Sections IV-C and V-B.

Imaging results are presented as vertical and horizontal slices at the tumor center coordinate in Fig. 3. All radar images are normalized according to the max energy voxel within the generated 3-D profile. In order to quantify the levels of background clutter, a signal-to-mean (S/Mn) metric is presented in Table I where the peak energy voxel is compared to the average energy within the imaged 3-D space. The permittivity ground truth slices are shown in Fig. 3(c) and (d). DAS results are presented

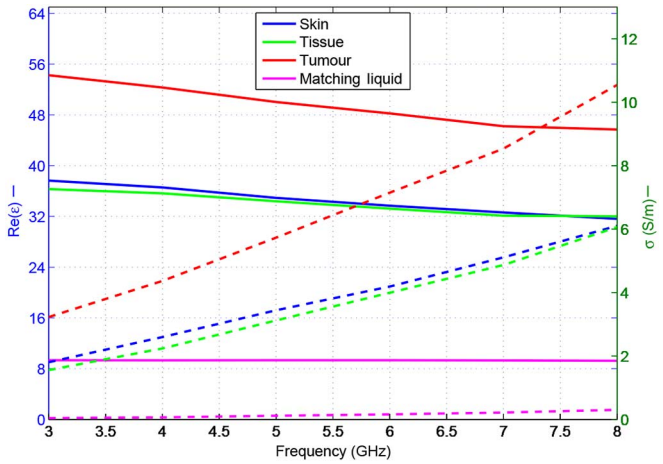

Fig. 6. Dielectric properties of phantom materials: solid lines represent permittivity and dashed lines represent conductivity.

in Fig. 3(e) and (f), while images generated by the wideband adaptive method are given in Fig. 3(g) and (h).

A twin target is evident for both methods as expected from differential rotation imaging [17]. Other residual scattering from the rotational process also presents, particularly for the glandular tissue region. From the images presented, the proposed wideband adaptive method improves the tumor response by minimizing the undesirable clutter. This is also reflected in the S/Mn results listed in Table I, where the wideband adaptive technique offers an improvement of over 5 dB when compared to the DAS output.

IV. EXPERIMENTAL VALIDATION

A. Data Acquisition

The algorithm is further evaluated using measurement data obtained from a 60-element antenna array operating as a bistatic radar system in the 4–8 GHz frequency range [30]. The full system consisting of a Rhode–Shwarz ZVT 8 port VNA and a custom designed switching matrix is shown in Fig. 4(b). The conformal array is populated with 60 wide-slot antennas [19] which are shown in Fig. 4(a). The system is designed to accommodate a patient in the prone position and prior to inserting the breast or phantom, the antennas are immersed in a matching liquid to mitigate skin reflections. The permittivity and conductivity of the liquid are 9.3 and 0.22 S/m, respectively, at 6 GHz.

Once the liquid is applied a custom low-loss ceramic cup is placed on top of the antenna array prior to the insertion of the breast or phantom [17]. The hemispherical cup has an outer radius of 86 mm, an inner radius of 66 mm, and is nondispersive with a permittivity of 10 and a loss tangent of 0.0005. This 20 mm padding provides a reasonable coverage of the breast from the wide-slot antenna radiation pattern.

B. Phantom Construction

Three phantoms are constructed to emulate skin contours and healthy tissue scattering regions within the breast. An initial phantom (I) is constructed to mimic a homogeneous imaging scenario. The skin phantom is a 1.5 mm uniform homogeneous liquid material encased within a matched ceramic cup,

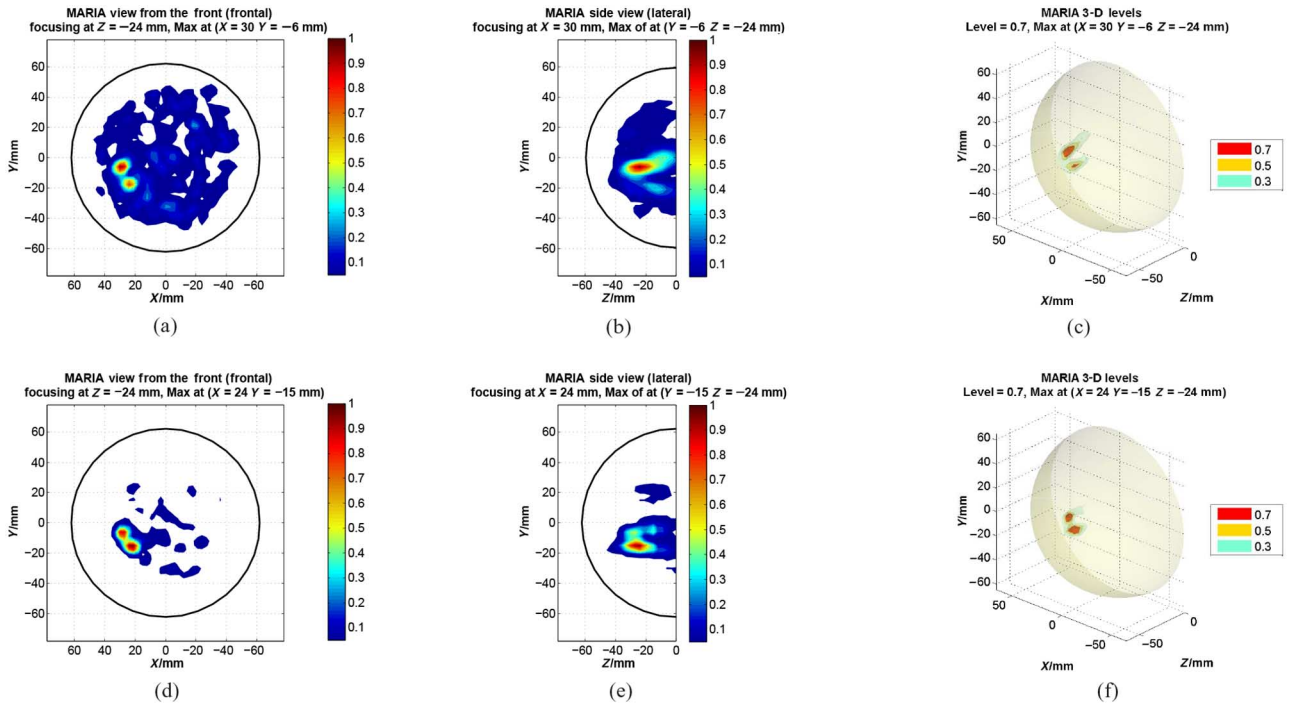

Fig. 7. Imaging results for Phantom I. (a) Two-dimensional (2-D) DAS frontal result. (b) 2-D DAS side view result. (c) 3-D DAS. (d) 2-D proposed algorithm frontal result. (e) 2-D proposed algorithm side view result. (f) 3-D proposed algorithm result.

as shown in Fig. 5(a). A 10 mm tumor target is placed at $(x = 20, y = -20, z = -25)$, as shown in Fig. 5(b). The chest-wall is accounted for by maintaining a liquid to air interface at the base of the breast phantom. The dielectric properties of each phantom material across the frequency range are shown in Fig. 6.

It was noted from a previous clinical study that the nonuniform contour of patient skin greatly affected the ability to localize suspicious regions within the breast [31]. Therefore, a nonuniform skin phantom was created using a Tx151-water mixture [17] to deliberately imitate a varying skin thickness between 1 and 3 mm, as shown in Fig. 5(c). At 6 GHz, the material has a dielectric constant of 32 and conductivity of 4.1 S/m. A piece of tissue mimicking material was created, shown in Fig. 5(d), which has a dielectric constant of 30 and a conductivity of 3.9 S/m. Phantom II includes a piece of tissue mimicking material, placed within the phantom at (20, 20, -12), while the tumour target is placed at $(-20, -20, -20)$. Finally, in phantom III, the target is located at (0, 20, -15) and tissue-mimicking material at (0, -30, -10).

C. Imaging Results

Imaging results for experiment I are shown in Fig. 7. In each figure, there are two 2-D slices shown, one offers a point-of-view slice from the anterior of the breast toward the chest wall and a lateral slice from the side. All energy levels are normalized relative to the maximum scattering energy in the reconstructed 3-D volume. Any scattering energy below 0.05 is not displayed in each 2-D slice. The third image is a 3-D scattering profile where energy levels above 0.3, 0.5, and 0.7 are shown to illustrate the level of overall clutter energy within the breast.

TABLE II
SIGNAL/MEAN METRIC RESULTS FOR THE PHANTOM EXPERIMENTS

Experiment	Signal/mean (dB)	
	Wideband adaptive	DAS
I	18.2	13.5
II	16.2	10.5
III	14.9	10.6

The wideband adaptive imaging method is shown to mitigate the presence of clutter which are evident within the DAS results in Fig. 7(a)–(c). A well-defined twin-target is observed in this case as a result of effective skin suppression from the array rotation technique. The images produced by the wideband adaptive method, shown in Fig. 7(d)–(f), show a visual improvement over the DAS results, with a well-defined twin-target presenting above 0.7 of the maximum energy. S/Mn results, given in Table II, are 4.7 dB greater for the wideband adaptive technique when compared to the DAS algorithm.

Fig. 8 describes the results of imaging experiment II for the DAS and wideband adaptive algorithm. The extraction of the breast scattering response no longer presents a twin-target due to the presence of the nonuniform skin layer and the additional piece of tissue-mimicking material. Within the DAS results, the level of clutter is more significant than in the case of experiment I. Conversly, the wideband adaptive method offers a significant improvement in clutter suppression, as evident in Fig. 8(d)–(f). S/Mn results are again significantly higher, registering a metric of 16.2 dB compared to the DAS performance of 10.8 dB.

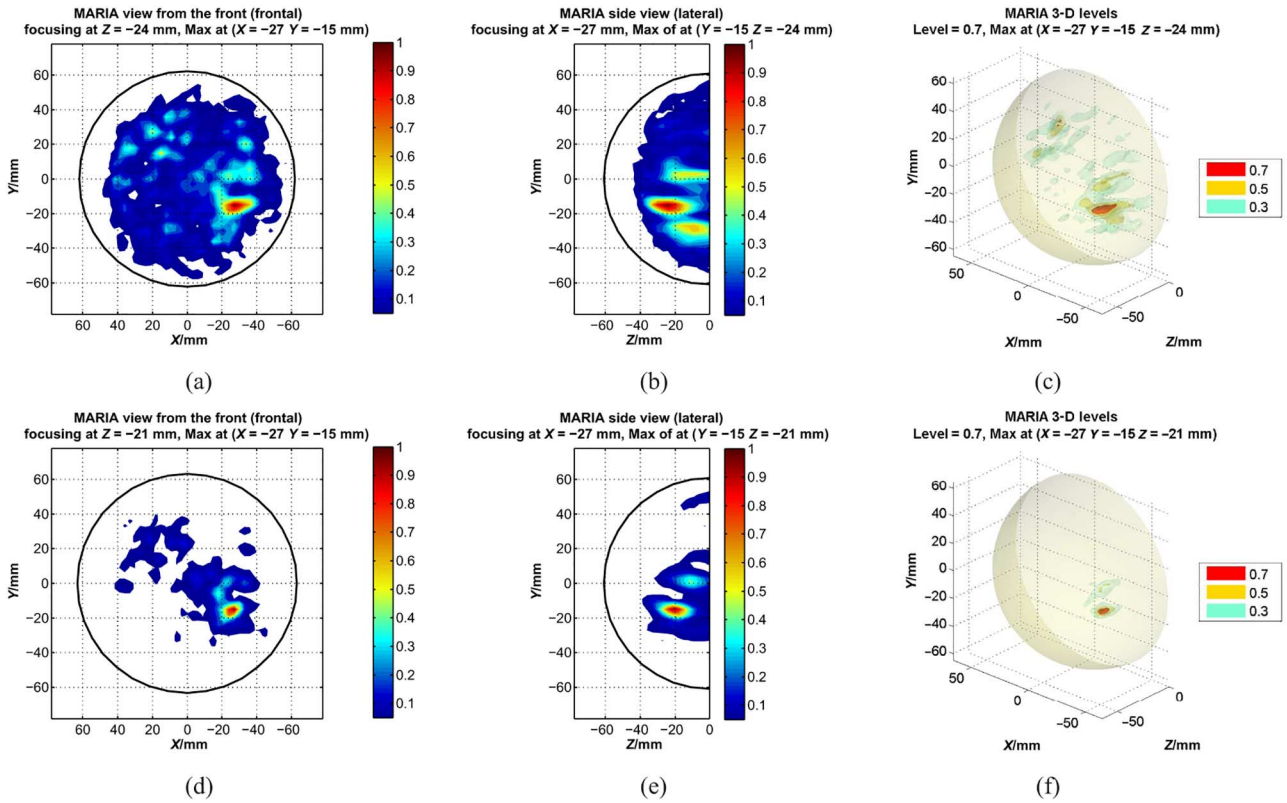

Fig. 8. Imaging results for Phantom II. (a) 2-D DAS frontal result. (b) 2-D DAS side view result. (c) 3-D DAS. (d) 2-D proposed algorithm frontal result. (e) 2-D proposed algorithm side view result. (f) 3-D proposed algorithm result.

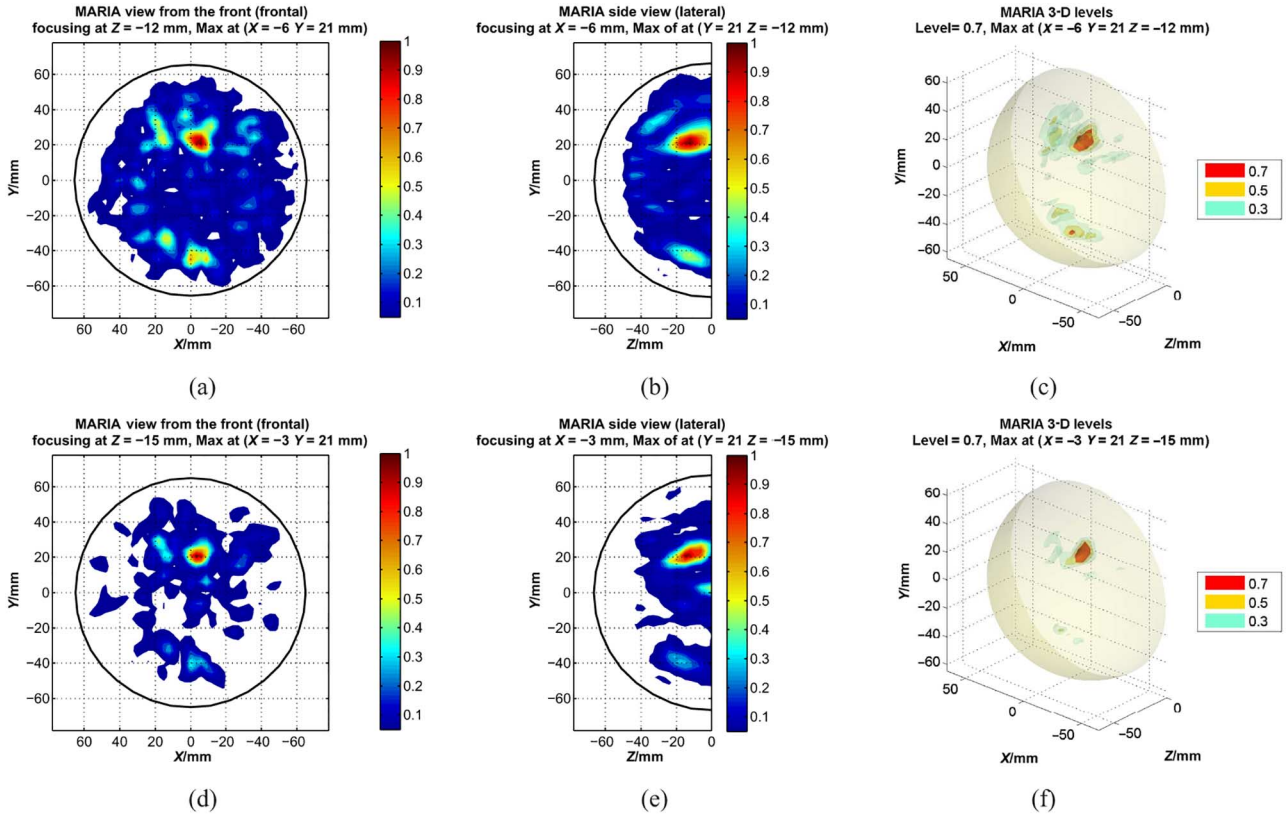

Fig. 9. Imaging results for Phantom III. (a) 2-D DAS frontal result. (b) 2-D DAS side view result. (c) 3-D DAS. (d) 2-D proposed algorithm frontal result. (e) 2-D proposed algorithm side view result. (f) 3-D proposed algorithm result.

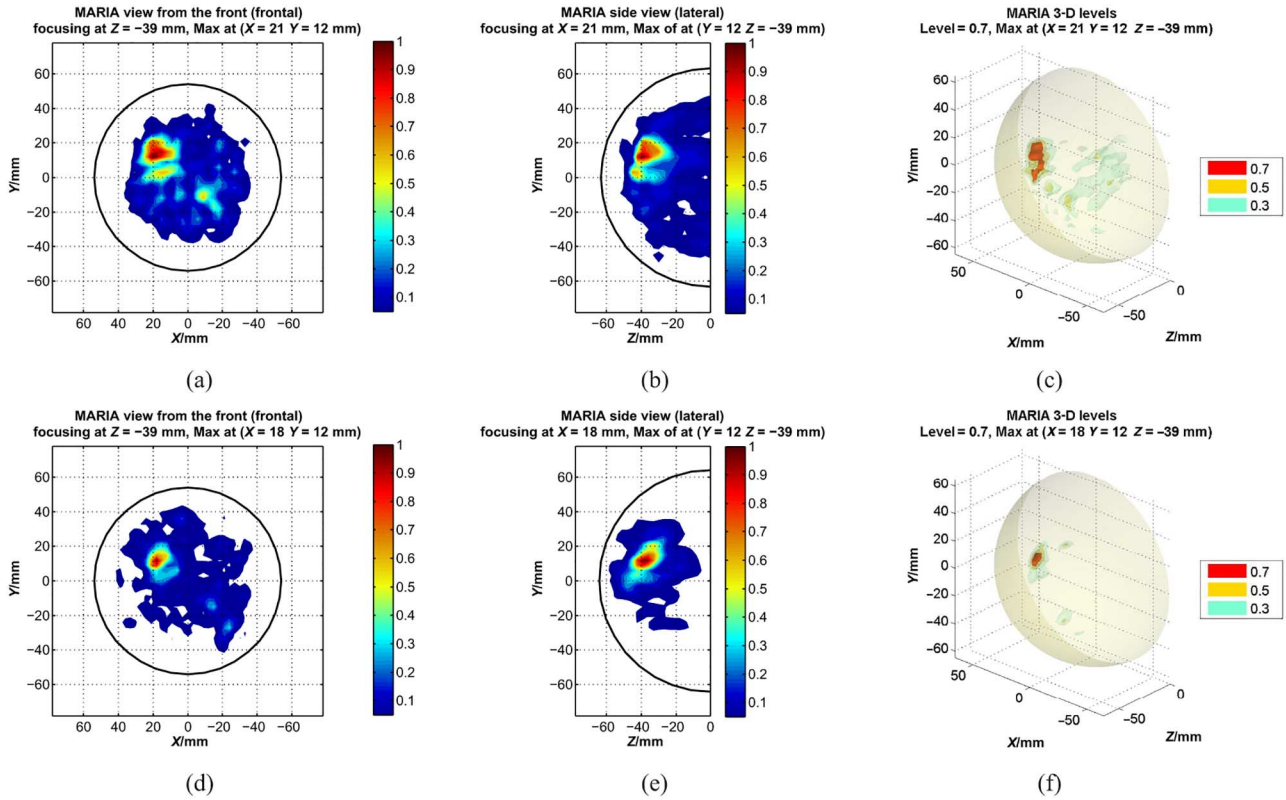

Fig. 10. Imaging results for clinical scan (P446). (a) 2-D DAS frontal result. (b) 2-D DAS side view result. (c) 3-D DAS. (d) 2-D proposed algorithm frontal result. (e) 2-D proposed algorithm side view result. (f) 3-D proposed algorithm result.

The results from experiment III, shown in Fig. 9, outline a significant relevant improvement for the proposed wideband adaptive technique over DAS. Clutter is greatly reduced in the output images, particularly in the 3-D profile shown in Fig. 9(f). There is a visual improvement evident in Fig. 9(d)–(f), with only the target and one small area near the inserted tissue-mimicking piece, registering above 0.5 of the peak energy. S/Mn ratio results are significantly greater than the DAS result, with an improvement of 4.8 dB using the wideband adaptive method.

Despite the lack of a twin target in experiments II and III, due to the inhomogeneity of the skin surface and the presence of an additional scatterer, the levels of clutter are reduced significantly. The reduction in S/Mn results for experiments II and III is due to the the inhomogeneity of both the skin phantom contour and the dielectric environment. Experiment III offers the lowest S/Mn ratio (14.9 dB) registered by the wideband adaptive technique; however, the target is located at a greater distance from the antennas and near the air (mimicking the chest) interface which can contribute undesirable backscatter.

V. Clinical Case

A. Data Acquisition

Clinical data were provided from trials that took place at Frenchay hospital during the first 6 months of 2011 [32] where patients underwent an X-ray examination, shown in Fig. 11, prior to microwave scanning. A suspicious region was identified above the nipple from the examination of the corresponding X-ray by a physician.

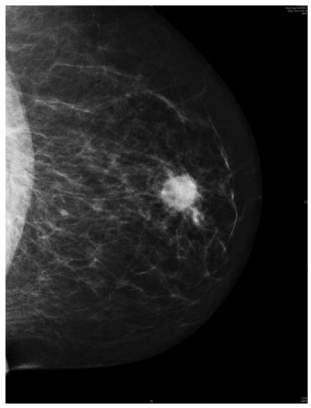

Fig. 11. Lateral X-ray for patient P446 with a suspicious region clearly evident.

B. Imaging Results

Fig. 10 illustrates the DAS output and the wideband adaptive method result using clinical data. The associated S/Mn metric results are outlined in Table III. Although the DAS algorithm identifies a large peak region (>0.7), there is still considerable clutter within the resulting images in Fig. 10(a)–(c). The wideband adaptive method produces a spherical peak region with an S/Mn result that is 3.8 dB greater than the DAS score. Due to the effects of X-ray compression, the authors acknowledge

TABLE III
SIGNAL/MEAN METRIC RESULTS FOR THE CLINICAL EXAMPLE

Patient	Signal/mean (dB)	
	Wideband adaptive	DAS
446	14.91	11.03

the difficulty to determine which result represents the tumour target in Fig. 11 more accurately. However, it is evident from the images shown in Fig. 10(d)–(f) that the levels of unwanted clutter energy are visibly reduced.

VI. CONCLUSION

Tumour target detection in radar imaging is often inhibited by the presence of clutter. In this paper, a data-adaptive imaging method has been applied in a wideband manner for the first time to create a representative microwave radar breast profile and reduce clutter. An equalization filter was detailed which compensates for the attenuation and phase errors resulting from propagation through the breast. A calculated permittivity estimate of the breast tissue was used to presteer and aid in the equalization process. The wideband adaptive method was evaluated in conjunction with the DAS method with a number of numerical and experimental measurement scenarios. A clinical breast radar scan was imaged to evaluate the algorithms performance with patient data. Resulting images were provided and a suitable metric was used to compare performance with the DAS method.

In all cases, numerical, experimental, and even clinical, the proposed wideband method significantly outperformed when compared to DAS. Energy profiles presented a clear visual improvement over the DAS algorithm and corresponding metric results highlighted an improvement of at least 3.8 dB.

REFERENCES

[1] N. Nikolova, "Microwave imaging for breast cancer," *IEEE Microw. Mag.*, vol. 12, no. 7, pp. 78–94, Dec. 2011.

[2] E. Fear, S. Hagness, P. Meaney, M. Okoniewski, and M. Stuchly, "Enhancing breast tumor detection with near-field imaging," *IEEE Microw. Mag.*, vol. 3, no. 1, pp. 48–56, Mar. 2002.

[3] P. Meaney, K. Paulsen, A. Hartov, and R. Crane, "Microwave imaging for tissue assessment: Initial evaluation in multitarget tissue-equivalent phantoms," *IEEE Trans. Biomed. Eng.*, vol. 43, no. 9, pp. 878–890, Sep. 1996.

[4] P. Meaney, M. Fanning, Q. Fang, and K. Paulsen, "Initial experience with a microwave imaging system for monitoring temperature change in an animal model," in *Proc. 23rd Annu. Int. Conf. IEEE Eng. Med. Biol. Soc.*, 2001, vol. 3, pp. 2844–2847.

[5] R. Benjamin, "Synthetic, post-reception focusing in near-field radar," in *Proc. EUREL Int. Conf. Detection Abandoned Land Mines: A Humanitarian Imperative Seeking Techn. Solution (Conf. Publ. No. 431)*, 1996, pp. 133–137.

[6] R. Benjamin *et al.*, "Microwave detection of buried mines using non-contact, synthetic near-field focusing," *IEE Proc. Radar Sonar Navig.*, vol. 148, no. 4, pp. 233–240, Aug. 2001.

[7] S. Hagness, A. Taflove, and J. Bridges, "Two-dimensional FDTD analysis of a pulsed microwave confocal system for breast cancer detection: Fixed-focus and antenna-array sensors," *IEEE Trans. Biomed. Eng.*, vol. 45, no. 12, pp. 1470–1479, Dec. 1998.

[8] B. Van Veen and K. Buckley, "Beamforming: A versatile approach to spatial filtering," *IEEE ASSP Mag.*, vol. 5, no. 2, pp. 4–24, Apr. 1988.

[9] R. Nilavalan, S. C. Hagness, and B. D. V. Veen, "Numerical investigation of breast tumour detection using multi-static radar," *IEE Electron. Lett.*, vol. 39, no. 25, pp. 1787–1789, Dec. 2003.

[10] X. Li and S. Hagness, "A confocal microwave imaging algorithm for breast cancer detection," *IEEE Microw. Wireless Compon. Lett.*, vol. 11, no. 3, pp. 130–132, Mar. 2001.

[11] E. Fear, X. Li, S. Hagness, and M. Stuchly, "Confocal microwave imaging for breast cancer detection: Localization of tumors in three dimensions," *IEEE Trans. Biomed. Eng.*, vol. 49, no. 8, pp. 812–822, Aug. 2002.

[12] E. Bond, X. Li, S. Hagness, and B. Van Veen, "Microwave imaging via space-time beamforming for early detection of breast cancer," *IEEE Trans. Antennas Propag.*, vol. 51, no. 8, pp. 1690–1705, Aug. 2003.

[13] X. Li, E. J. Bond, B. D. Van Veen, and S. C. Hagness, "An overview of ultra-wideband microwave imaging via space-time beamforming for early-stage breast-cancer detection," *IEEE Antennas Propog. Mag.*, vol. 47, no. 1, pp. 19–34, Feb. 2005.

[14] M. O'Halloran, E. Jones, and M. Glavin, "Quasi-multistatic MIST beamforming for the early detection of breast cancer," *IEEE Trans. Biomed. Eng.*, vol. 57, no. 4, pp. 830–840, Apr. 2010.

[15] H. L. Van Trees, Ed., *Optimum Array Processing (Detection, Estimation, and Modulation Theory, Part IV)*. Hoboken, NJ, USA: Wiley, 2002, no. 50.

[16] Y. Xie, B. Guo, L. Xu, J. Li, and P. Stoica, "Multistatic adaptive microwave imaging for early breast cancer detection," *IEEE Trans. Biomed. Eng.*, vol. 53, no. 8, pp. 1647–1657, Aug. 2006.

[17] M. Klemm, I. Craddock, J. Leendertz, A. Preece, and R. Benjamin, "Radar-based breast cancer detection using a hemispherical antenna array—Experimental results," *IEEE Trans. Antennas Propag.*, vol. 57, no. 6, pp. 1692–1704, Jun. 2009.

[18] M. Lazebnik *et al.*, "A large-scale study of the ultrawideband microwave dielectric properties of normal breast tissue obtained from reduction surgeries," *Phys. Med. Biol.*, vol. 52, pp. 2637–2656, 2007.

[19] D. Gibbins *et al.*, "A comparison of a wide-slot and a stacked patch antenna for the purpose of breast cancer detection," *IEEE Trans. Antennas Propag.*, vol. 58, no. 3, pp. 665–674, Mar. 2010.

[20] M. Sarafianou *et al.*, "MUSIC processing for permittivity estimation in a delay-and-sum imaging system," in *Proc. 2013 7th Eur. Conf. Antennas Propag. (EuCAP)*, 2013, pp. 839–842.

[21] M. Lazebnik *et al.*, "A large-scale study of the ultrawideband microwave dielectric properties of normal, benign and malignant breast tissues obtained from cancer surgeries," *Phys. Med. Biol.*, vol. 52, pp. 6093–6115, 2007.

[22] B. Van Veen and K. Buckley, *Digital Signal Processing Handbook*, V. Madisetti and D. Williams, Eds., Boca Raton, FL, USA: CRC Press, 1998, pp. 61-1–61-21.

[23] S. Vorobyov, A. Gershman, and Z.-Q. Luo, "Robust adaptive beamforming using worst-case performance optimization: A solution to the signal mismatch problem," *IEEE Trans. Signal Process.*, vol. 51, no. 2, pp. 313–324, Feb. 2003.

[24] B. Carlson, "Covariance matrix estimation errors and diagonal loading in adaptive arrays," *IEEE Trans. Aerosp. Electron. Syst.*, vol. 24, no. 4, pp. 397–401, Jul. 1988.

[25] M. Rubsamen and A. Gershman, "Robust presteered broadband beamforming based on worst-case performance optimization," in *Proc. 5th IEEE Sens. Array Multichannel Signal Process. Workshop (SAM'08)*, 2008, pp. 340–344.

[26] J. Li, P. Stoica, and Z. Wang, "On robust capon beamforming and diagonal loading," *IEEE Trans. Signal Process.*, vol. 51, no. 7, pp. 1702–1715, Jul. 2003.

[27] A. El-Keyi, T. Kirubarajan, and A. Gershman, "Wideband robust beamforming based on worst-case performance optimization," in *Proc. IEEE/SP 13th Workshop Statist. Signal Process.*, 2005, pp. 265–270.

[28] S. A. Vorobyov, "Principles of minimum variance robust adaptive beamforming design," *Signal Process.*, vol. 93, no. 12, pp. 3264–3277, Dec. 2013.

[29] E. Zastrow *et al.*, "Development of anatomically realistic numerical breast phantoms with accurate dielectric properties for modeling microwave interactions with the human breast," *IEEE Trans. Biomed. Eng.*, vol. 55, no. 12, pp. 2792–2800, Dec. 2008.

[30] M. Klemm *et al.*, "Development and testing of a 60-element UWB conformal array for breast cancer imaging," in *Proc. 5th Eur. Conf. Antennas Propag. (EUCAP)*, 2011, pp. 3077–3079.

[31] M. Klemm *et al.*, "Clinical trials of a UWB imaging radar for breast cancer," in *Proc. 4th Eur. Conf. Antennas Propag. (EuCAP)*, 2010, pp. 1–4.

[32] T. Henriksson *et al.*, "Clinical trials of a multistatic UWB radar for breast imaging," in *Proc. Loughborough Antennas Propag. Conf. (LAPC'11)*, 2011, pp. 1–4.

Dallan Byrne received the B.Eng. degree in electronic and computer engineering and the Ph.D. degree in cancer detection using ultrawide-band radar techniques from the National University of Ireland, Galway, in 2007 and 2012, respectively.

Since 2012, he has been a Research Assistant with the University of Bristol, U.K. As a member of the microwave breast imaging team, his work focuses on the advancement of radar and DSP techniques for clinical breast scanning. His research interests include microwave and radar imaging, and the biomedical application of signal processing techniques.

Ian J. Craddock is a full Professor with the University of Bristol, U.K. and the Director of the flagship "SPHERE IRC. He has been working in RF medical imaging for 10 years and he founded a company that is currently completing regulatory approval of a commercial RF breast imaging device. He has authored over 100 papers. He serves on the Steering Board of the University's Health Research Institute. He is also separately employed with Telecommunications Research Lab, Toshiba, Bristol, U.K., as Managing Director, responsible for a portfolio of both internal and collaborative communications, healthcare, and smart city research.